Grid-Forming Vector Current Control

Mario Schweizer, *Member, IEEE*, Stefan Almér, Sami Pettersson, *Member, IEEE*, Arvid Merkert, *Member, IEEE*, Vivien Bergemann, and Lennart Harnefors, *Fellow, IEEE*

***Abstract*—In this article, a novel point of view on grid-forming control with current controlled power electronic converters is presented. A control concept based on the emulation of the combined effect of a virtual synchronous condenser and a parallel-connected virtual current source is proposed. It combines the positive effects of virtual synchronous generator control, such as the provision of inertia, voltage support, the possibility of islanded operation, and good control performance in weak grids, with the benefits of vector current control, such as fast current limitation, improved synchronization properties, and fast setpoint tracking. The proposed control concept is simply a modification of standard vector current control. Therefore, it can be implemented easily on all control platforms with minor software changes. The control method is verified with analytical models, time-domain simulations, and experimental results.**

***Index Terms*—Phase locked loop, virtual inertia, virtual synchronous generator.**

I. Introduction

THE transmission and distribution grid is currently undergoing a transition where conventional synchronous generation is being displaced by converter-interfaced renewable energy resources. It has been shown in many studies that there is a risk of grid instability if the utility grid is equipped with a high amount of converter-interfaced energy resources that do not employ any grid supporting control strategy [1], [2].

Novel converter control strategies can mitigate the risk of instability. There are a number of unique characteristics of such control methods. Most important is the ability to adapt and share the amount of injected active power according to the demand of the various loads in real-time. This is achieved with a terminal behavior that resembles a voltage source with a low output impedance. Furthermore, such control methods aim to provide "virtual inertia" to the grid, meaning that the rate of change of the grid frequency is limited. The combined effect of voltage source characteristics and inertia leads to characteristics that are very close to the behavior of a synchronous generator.

Converter-interfaced energy resources with grid-forming control methods are able to fully replace conventional synchronous generators in the grid. It is possible to operate a grid without any conventional synchronous generator connected to it, a situation that has become common, e.g., in microgrids or in railway grids already.

Today's control methods that can provide grid support are predominantly based on two basic concepts, the droop control [3], [4] and the virtual synchronous generator [5], [6] concept.

History of grid supporting converter control started in the 1980s with first attempts to support the grid with a battery energy storage system (BESS) [7]. Droop control was introduced in [8] for the operation of parallel connected converters supplying a stand-alone ac system. In many applications, it is required to connect several converter units in parallel in order to increase the nominal power of the system. Consequently, the proposed concept was applied to control parallel connected uninterruptible power supply (UPS) units [9], parallel connected BESS converters [10], and parallel connected photovoltaic (PV) inverter units [11] a few years later.

The initially proposed droop control concept has been improved with several extensions over time, such as virtual impedance [12]–[14], or methods to emulate inertia and damping effect [15].

A completely new concept was introduced around 2007 with the idea of emulating the behavior of synchronous generators or synchronous machines with the converter control. Several implementation variants have been proposed, such as the virtual synchronous machine (VISMA, VSM) [16] or the virtual synchronous generator (VSG) [17]. The two concepts mainly vary in the complexity, i.e., the order of the adopted machine equations. Both concepts originally have been based on current references that are calculated with the machine equations and subsequently tracked with current controllers. A reformulation of the concept to create voltage references instead of current references was given in [18].

A further voltage reference-based virtual machine concept was introduced in [19], known as the Synchronverter concept. It simplifies the control method by assuming that the converter filter inductance is equivalent to the stator impedance of the VSM. In a later publication, the possibility to adapt the output impedance with a virtual stator impedance was reintroduced [20]. A similar control method known as power synchronization control was presented in [21]. It can improve the control performance of converters that are connected to weak grids.

Manuscript received 10 December 2021; revised 3 March 2022 and 26 April 2022; accepted 13 May 2022. Date of publication 26 May 2022; date of current version 26 July 2022. Recommended for publication by Associate Editor A. Yazdani. *(Corresponding author: Mario Schweizer.)*

Mario Schweizer and Sami Pettersson are with the ABB Corporate Research, 5405 Baden-Dättwil, Switzerland (e-mail: mario.schweizer@ch.abb.com; sami.pettersson@ch.abb.com).

Stefan Almér is with the Totalförsvarets forskningsinstitut (FOI), 16440 Gullfossgatan, Sweden (e-mail: almer@math.kth.se).

Arvid Merkert and Vivien Bergemann are with the ABB Automation GmbH, 21079 Hamburg, Germany (e-mail: arvid.merkert@de.abb.com; vivien.bergemann@de.abb.com).

Lennart Harnefors is with the ABB Corporate Research, 72178 Västeras, Sweden (e-mail: lennart.harnefors@se.abb.com).

Color versions of one or more figures in this article are available at https://doi.org/10.1109/TPEL.2022.3177938.

Digital Object Identifier 10.1109/TPEL.2022.3177938

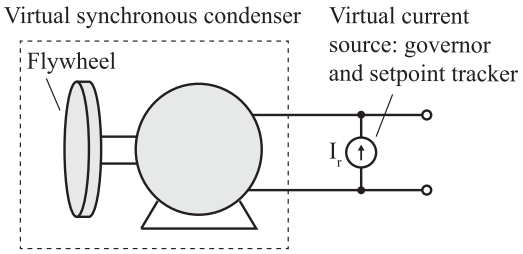

Fig. 1. Basic concept of GFVCC.

Several papers discuss the similarities between droop control and virtual generator control [5], [15]. It was concluded that the two concepts are more or less equivalent.

The existing control solutions have several shortcomings such as high complexity and difficult tuning approach with high commissioning effort [22]. Therefore, a search for simplified control concepts offering the same advantages as VSM control regarding grid supporting capabilities and being at the same time as simple as the well-known current control strategies, such as vector current control, has started several years ago.

A simplified method to emulate only the low frequency characteristics of a synchronous generator is the provision of virtual inertia using a standard current control scheme and an extra power reference term calculated with the derivative of the measured frequency [23]–[25], known as df/dt based inertia emulation. However, the performance of the method depends heavily on the filter used for frequency measurement and its short term ($t < 10$ ms) response on load steps is different compared to virtual synchronous generators.

Another approach is the idea to merge the swing equation, which describes the low frequency characteristics of synchronous machines, with the phase-locked-loop (PLL) unit, which is often used to synchronize conventional current control schemes with the grid voltage. First attempts have been shown in [26]–[28]. It has been shown that the PLL can reproduce certain characteristics of the swing equation if it is tuned properly. Similar findings have been presented in [29], where an inertia-like effect of the PLL in vector current control was found. However, a systematic analysis as well as a clear link between the PLL and VSM equations, including damper winding emulation and virtual stator impedance, has been missing.

In this article, a novel point of view on grid-forming behavior with current controlled converters is presented. The proposed concept is named grid-forming vector current control (GFVCC). It is based on the emulation of the combined effect of a virtual synchronous condenser and a parallel connected virtual current source according to Fig. 1. The concept is simply an add-on to standard vector current control with PLL and can therefore be implemented easily on all control platforms with minor software modifications. It improves upon the concepts in [26]–[28] due to correct emulation of damper winding and virtual stator impedance and conceptual separation of transient and steady-state response. It has the following main advantages.

1) Compared to VSM implementations with cascaded voltage and current control loops [30], the proposed method is less complex. Due to the removal of the voltage control stage and the integration of the swing equation into the PLL, the number of control tuning parameters reduces considerably and the commissioning effort is minimized.
2) Potentially improved synchronization characteristics during faults and inherent overcurrent handling. Conventional VSM control with cascaded voltage and current control loops is known that it can lose synchronism with the grid during faults and has difficulties to resynchronize (cf., [31]). Also, PLL-based current control can lose synchronism during grid faults but several options to improve the behavior exist, such as freezing the PLL frequency or the usage of an adaptive PLL (cf., [32]).
3) Compared with the current-controlled VISMA method, GFVCC is based on standard pulsewidth modulation instead of hysteresis current control. The VISMA method has issues in stand-alone operation without load and needs hardware modifications (i.e., output capacitors are required) to work properly [18]. This is not the case with GFVCC.
4) Compared with the df/dt based inertia emulation scheme, GFVCC emulates additionally the low output impedance characteristic of a synchronous generator which is important for sinking/sourcing of harmonics, for providing reactive power, and for fast power injection during load-steps. Furthermore, the df/dt method requires elaborate tuning of the frequency measurement low-pass filter to make it run in stand-alone mode [33].

The proposed control concept is suitable for the control of utility grade battery energy storage systems [34] providing virtual inertia. Furthermore, it enables grid-forming functionality for microgrid applications, railway interties, and high-voltage dc (HVDC) stations [35], as well as for future static synchronous compensators and HVDC stations with integrated storage [36], [37].

The rest of this article is organized as follows. In Section II, the swing equation-based formulation of VSM control is reviewed as a starting point. In Section III, the analytical derivation of the control concept is given. It is shown that the VSM swing equation including damper winding emulation and virtual stator impedance can be reproduced accurately with special tuning rules for a standard PLL and a virtual admittance block creating VSM-equivalent current references. In Section IV, it is shown that the control scheme is compatible with the recently proposed generalized PLL-based grid-forming control framework. In Section V, a possible implementation of the control method is presented. Simulation results for several scenarios are shown and discussed in Section VI. Experimental results obtained with two 25 kW inverter units are presented in Section VII. Finally, Section VIII concludes this article.

II. Swing Equation-Based VSM Formulation

The goal of VSM control is to make the behavior of the converter at the point of common coupling (PCC) equal to the behavior of a synchronous machine (cf., Fig. 2). The simplest method to achieve such a behavior is to control the converter output voltage according to the swing equation.

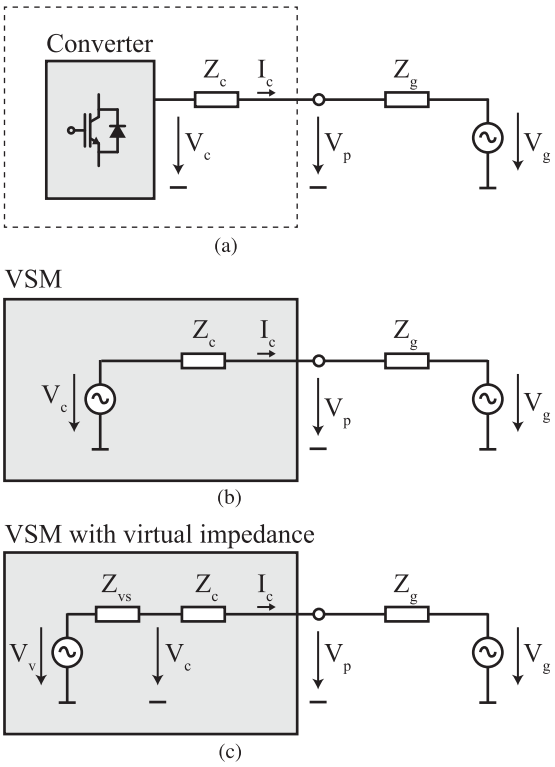

Fig. 2. Equivalent models of a swing equation-based VSM. (a) VSI, (b) VSM without virtual stator impedance, (c) VSM with virtual stator impedance.

The following derivations are based on a converter with an inductive output filter for simplicity reasons. Furthermore, the resistive parts of the considered impedances are neglected, i.e., ($Z = R + j\omega L = R + jX \approx jX$).

The proposed control concept can be applied to converters with *LCL* filter if the current control is configured to dampen the filter resonances as shown in Section V. However, multistage filters in *LC* or *LCL* configuration change the behavior at the PCC as they introduce additional dynamics. The exact behavior with such filters has not been studied yet.

The swing equation couples the change of frequency of the back electromotive force (EMF) with the output power of the machine. In the case of a VSM without virtual stator impedance, the converter voltage V_c is set to be equal to the back EMF of the virtual machine. The converter filter impedance Z_c is equal to the stator impedance of the virtual machine and the PCC voltage V_p is equal to the stator voltage of the virtual machine. The converter voltage V_c has the rotational frequency ω_r to highlight its equivalency with the virtual rotor frequency. The PCC voltage (virtual stator voltage) has the rotational frequency ω_p. The swing equation can be formulated as

$$M\frac{d\omega_r}{dt} = \overbrace{-P_{\text{out}}}^{\text{output power}} - \overbrace{K_f(\omega_r - \omega_p)}^{\text{damping}} + \overbrace{P_{\text{set}} - K_g(\omega_r - \omega_{\text{set}})}^{\text{governor power}} \tag{1}$$

$$\frac{d\theta_r}{dt} = \omega_r. \tag{2}$$

M denotes the virtual inertia, K_f the damper winding constant, K_g the droop constant, P_{set} and ω_{set} the power and angular frequency setpoints of the speed governor. In the quasi-steady state, the output power is given by the angle difference between the virtual back EMF V_c and the PCC voltage V_p across the converter filter reactance

$$P_{\text{out}} = c_p \frac{V_c V_p}{X_c} \sin(\theta_r - \theta_p). \tag{3}$$

The constant c_p is related to the power calculation and is given with $c_p = 3$ for three-phase systems and rms phase voltages. (If the peak phase voltages are used instead, $c_p = 3/2$). Equation (1) can be rewritten as

$$\frac{d\omega_r}{dt} = -c_p \frac{V_c V_p}{M X_c} \sin(\theta_r - \theta_p) - \frac{K_f}{M}(\omega_r - \omega_p) + \frac{1}{M}P_{\text{set}} - \frac{K_g}{M}(\omega_r - \omega_{\text{set}}). \tag{4}$$

Modern power electronic converters are designed with minimized filtering components. The filter inductance is much lower compared to a stator inductance of a generator in a p.u. sense. This leads to uneven short-term power sharing and oscillatory control if the voltage reference-based VSM control method is applied without a virtual output impedance. Therefore, state-of-the-art VSM implementations have introduced a virtual stator impedance according to Fig. 2(c).

The virtual stator reactance changes the equations slightly. The converter voltage V_c in phasor notation is calculated according to

$$V_c = V_v - jX_{\text{vs}} I_c. \tag{5}$$

Now, the virtual back EMF of the machine is designated as V_v (with rotational frequency ω_r and angle θ_r). Regarding the behavior at the PCC, the virtual machine has now a total virtual stator reactance of $X_v = X_c + X_{\text{vs}}$ and the power equation changes to

$$P_{\text{out}} = c_p \frac{V_v V_p}{X_{\text{vs}} + X_c} \sin(\theta_r - \theta_p) = c_p \frac{V_v V_p}{X_v} \sin(\theta_r - \theta_p). \tag{6}$$

Equation (4) becomes

$$\frac{d\omega_r}{dt} = -c_p \frac{V_v V_p}{M X_v} \sin(\theta_r - \theta_p) - \frac{K_f}{M}(\omega_r - \omega_p) + \frac{1}{M}P_{\text{set}} - \frac{K_g}{M}(\omega_r - \omega_{\text{set}}). \tag{7}$$

It should be noted that the virtual inductance L_{vs} is connected in series to the converter filter inductance L_c, and therefore, adds to the total virtual stator inductance of the virtual machine seen from the PCC.

III. Analytical Derivation of GFVCC

A. Basic Concept

The proposed control concept can be separated into two functional parts: a virtual synchronous condenser that is connected in parallel with a virtual current source [cf., Fig. 3(b)]. Both parts

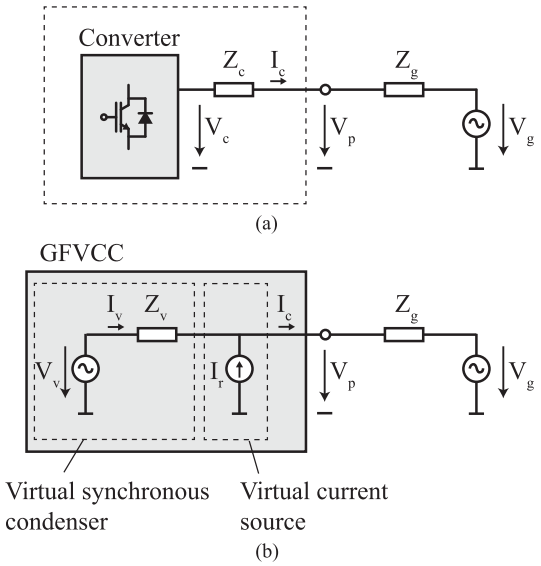

Fig. 3. Equivalent models of (a) VSI and (b) grid-forming vector current control.

are emulated by the control scheme and create individual current references which are superimposed and impressed by standard current control.

A synchronous condenser is a synchronous generator without mechanical input power, i.e., it behaves as a spinning wheel. In the steady state, it injects only reactive power and supports the bus voltage magnitude. During grid transients, it injects active power for a short period of time that is known as inertial power injection. The behavior of the virtual condenser is emulated with the PLL and a virtual admittance block that creates the respective current references.

The purpose of the virtual current source is twofold. It is used as a power setpoint tracker and it replaces the governor of a traditional synchronous generator. It ensures steady-state power balance between the grid and the spinning wheel. In the steady state, the complete active power to the grid is injected by the virtual current source.

B. Equivalency of PLL and Swing Equation

In the proposed control scheme, the swing equation is not directly implemented as in traditional approaches. Moreover, the effect of the PLL together with the virtual admittance is compared to the swing equation. The angle θ_r is no longer computed by the swing equation, but it is the output of the PLL. With $s = d/dt$, the PLL equations are given as

$$\begin{aligned}\omega_r &= \left(K_{\mathrm{pll,p}} + \frac{K_{\mathrm{pll,i}}}{s}\right) V_{\mathrm{p,q}} \\ &= -\left(K_{\mathrm{pll,p}} + \frac{K_{\mathrm{pll,i}}}{s}\right) V_p \sin(\theta_r - \theta_p) \qquad (8)\end{aligned}$$

$$\theta_r = \int \omega_r dt. \qquad (9)$$

Taking the derivative of the first equation, we get

$$\frac{d\omega_r}{dt} = -(sK_{\mathrm{pll,p}} + K_{\mathrm{pll,i}}) V_p \sin(\theta_r - \theta_p). \qquad (10)$$

For small angle differences, which is the case for reasonable loading conditions, the sine function can be approximated as $\sin(\theta_r - \theta_p) \approx \theta_r - \theta_p$ and the derivative thereof becomes $s \cdot \sin(\theta_r - \theta_p) \approx \omega_r - \omega_p$. We can therefore rewrite the equation set as

$$\frac{d\omega_r}{dt} = -K_{\mathrm{pll,i}} V_p \sin(\theta_r - \theta_p) - K_{\mathrm{pll,p}} V_p (\omega_r - \omega_p) \qquad (11)$$

$$\frac{d\theta_r}{dt} = \omega_r. \qquad (12)$$

By comparing this equation set with the swing equation with virtual stator impedance [cf., (7)], we can find the PLL gains for formal equivalence as follows:

$$K_{\mathrm{pll,p}} = \frac{K_f}{M V_p} \qquad (13)$$

$$K_{\mathrm{pll,i}} = c_p \frac{V_v}{M X_v}. \qquad (14)$$

The governor power is still missing but will be replaced in a later step with the virtual current source. The proportional gain of the PLL, therefore, emulates the damper winding effect and the integral gain couples the angle difference with an increase/decrease of frequency, emulating the self-synchronization principle of synchronous machines.

As opposed to the swing equation, the PLL does not implicitly couple the output power with the angle difference, because it describes only the evolution of the internal PLL angle ω_r. Coupling of output power and angle difference has to be ensured explicitly with an additional current reference given to the current controller. Similar as in the virtual synchronous machine, the missing piece that couples the output power with the evolution of the PLL angle is the virtual stator impedance. The stator impedance is assumed to be of RL-type and is given as a dq-frame impedance matrix

$$Z_v(s) = \begin{bmatrix} R_v + sL_v & -\omega_N L_v \\ \omega_N L_v & R_v + sL_v \end{bmatrix}. \qquad (15)$$

ω_{N} is the nominal angular frequency of the grid. The current reference is created with a virtual admittance being equivalent to the inverse of the virtual stator impedance

$$Y_v(s) = Z_v(s)^{-1}. \qquad (16)$$

The current references $i_{\mathrm{v,dq}}$ are calculated with the matrix multiplication of the virtual admittance with the voltage difference between a virtual back EMF voltage V_v and the PCC voltage V_p. The virtual back EMF is always aligned to the d-direction of the PLL reference frame [cf., Fig. 4].

The individual components of the current reference in d- and q-directions are calculated with

$$i_{\mathrm{v,d}} = Y_{\mathrm{v,dd}}(s)(V_v - V_{\mathrm{p,d}}) + Y_{\mathrm{v,dq}}(s)(-V_{\mathrm{p,q}}) \qquad (17)$$

$$i_{\mathrm{v,q}} = Y_{\mathrm{v,qd}}(s)(V_v - V_{\mathrm{p,d}}) + Y_{\mathrm{v,qq}}(s)(-V_{\mathrm{p,q}}). \qquad (18)$$

We have established current references, which are equivalent to the currents that are injected automatically if the converter output voltage is controlled by the swing equation with a virtual stator impedance.

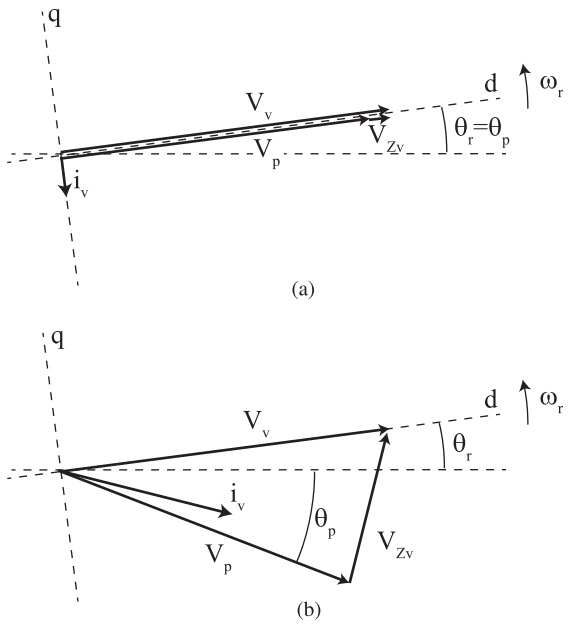

Fig. 4. Vector diagram for the virtual synchronous condenser part of the control concept in (a) the steady state and (b) during a transient situation.

In order to show equivalency with the active power injected by the swing equation, we assume again quasi-steady-state conditions ($s = 0$, $\omega_N L_v = X_v$) and negligible virtual stator resistance ($R_v \ll X_v$). In that case, the virtual admittance matrix simplifies to

$$Y_v \approx \begin{bmatrix} 0 & \frac{1}{X_v} \\ -\frac{1}{X_v} & 0 \end{bmatrix} \tag{19}$$

and the current references become

$$i_{\mathrm{v,d}} = -\frac{1}{X_v} V_{\mathrm{p,q}} \tag{20}$$

$$i_{\mathrm{v,q}} = \frac{1}{X_v}(V_{\mathrm{p,d}} - V_v). \tag{21}$$

Assuming sufficiently fast tracking of the current references by the controller, the injected power is given by

$$\begin{aligned} P_{\text{out}} &= c_p(V_{\mathrm{p,d}} i_{\mathrm{v,d}} + V_{\mathrm{p,q}} i_{\mathrm{v,q}}) \\ &= c_p\left(-\frac{V_{\mathrm{p,d}} V_{\mathrm{p,q}}}{X_v} + \frac{V_{\mathrm{p,q}} V_{\mathrm{p,d}}}{X_v} - \frac{V_v V_{\mathrm{p,q}}}{X_v}\right) \\ &= c_p \frac{V_v V_p}{X_v} \sin(\theta_r - \theta_p). \end{aligned} \tag{22}$$

We have therefore ensured equivalence between the quasi-steady-state output power governed by the swing equation and the output power created by the PLL + virtual admittance combination.

Different to the traditional VSM implementation, the combination of PLL and virtual admittance just emulates a spinning wheel without a governor for the mechanical input power. Therefore, the injected active power from the spinning wheel will be zero in the steady state and the angle θ_r aligns with θ_p as shown in Fig. 4(a). The behavior can be explained by considering the PLL integrator. In the steady state, it always enforces $V_{\mathrm{p,q}} = 0$, and therefore, the active power current component will be $i_{\mathrm{v,d}} = -V_{\mathrm{p,q}}/X_v = 0$ as well. If there is a difference in the voltage magnitudes, reactive power will be injected with a reactive power current component of $i_{\mathrm{v,q}} = (V_{\mathrm{p,d}} - V_{\mathrm{v}})/X_v$.

The situation is different during severe grid transients, e.g., a tripping of a large power plant. Such events typically result in bus voltage angle step changes with a subsequent grid frequency change. Due to the low bandwidth of the PLL, the PLL angle θ_r will not be aligned with the PCC voltage angle θ_p temporarily as shown in Fig. 4(b). As a result, $V_{\mathrm{p,q}}$ is not equal to zero and active power will be injected temporarily, until the transient situation has settled again.

The virtual admittance ideally is implemented with the full dynamic model to ensure passivity and damping of high frequency resonances.

It has been shown that the combination of special settings for the PLL gains and a virtual admittance allows to emulate the effect of inertia, damper winding, and stator impedance of a virtual synchronous machine with the conventional control structure used for vector current control.

C. Speed Governor Control

The speed governor effect (droop control loop) is emulated with the virtual current source, i.e., with an additional current reference component. It ensures that a power component equivalent to the effect of the speed governor is injected, maintaining the power balance in steady state. The complete control block diagram is shown in Fig. 7.

The additional current reference is calculated with

$$i_{\mathrm{r,d}} = \frac{P_{\text{set}} - K_g(\omega_r - \omega_{\text{set}})}{c_p V_{\mathrm{p,d}}} \tag{23}$$

which leads to an injected power of

$$P_g = c_p V_{\mathrm{p,d}} i_{\mathrm{r,d}} = P_{\text{set}} - K_g(\omega_r - \omega_{\text{set}}). \tag{24}$$

In the steady state, the angle difference $\theta_r - \theta_p$ is always zero and $V_{\mathrm{p,d}} \approx V_N$. Therefore, the division by $V_{\mathrm{p,d}}$ can be replaced with a division by constant V_N

$$i_{\mathrm{r,d}} = \frac{P_{\text{set}} - K_g(\omega_r - \omega_{\text{set}})}{c_p V_N}. \tag{25}$$

If very accurate tracking of the power set-point is required in situations where the magnitude of the PCC voltage can deviate from the nominal voltage V_N, it is recommended to replace the division by V_N with a division by $|V_p|$ processed with a low-pass filter having a low cutoff frequency ($f_c < 5$ Hz).

The d-component of the current reference given to the current controller is given as

$$i_d{}^* = i_{\mathrm{r,d}} + i_{\mathrm{v,d}}. \tag{26}$$

D. Optional Control Blocks

1) Automatic Voltage Regulator (AVR): The emulated VSM naturally injects a certain amount of reactive power in response to a change in the bus voltage magnitude, basically limited by

the virtual reactance. However, often an additional bus voltage regulation is required. There are basically two different ways how a typical AVR could be implemented in the presented control structure. With the first method, the virtual back EMF V_v is directly manipulated in order to increase or decrease the injected reactive power of the virtual synchronous condenser. With the second method, an additional q-current component can be injected to change the reactive power, e.g., with a voltage droop curve.

In this work, the second approach is followed. The current reference is given as

$$i_{\mathrm{r,q}} = -\frac{Q_{\mathrm{set}} - G_{\mathrm{avr}}(s)(|V_p| - V_{\mathrm{set}})}{c_p V_N}. \tag{27}$$

Q_{set} and V_{set} denote the reactive power and voltage setpoints of the AVR. Typically, $V_{\mathrm{set}} = V_v$ is chosen. Because the current source-based AVR will complement the reactive power injected by the virtual synchronous condenser, it is suggested to design the AVR control loop with rather low bandwidth. A voltage droop curve with droop constant K_{Vd} and a first order low-pass filter with $\omega_0 = 0.05 \cdot \omega_N$ have been implemented

$$G_{\mathrm{avr}}(s) = K_{\mathrm{Vd}} \cdot G_{\mathrm{lp}}(s). \tag{28}$$

The q-component of the current reference given to the current controller is modified to

$$i_q{}^* = i_{\mathrm{r,q}} + i_{\mathrm{v,q}}. \tag{29}$$

2) Low-Pass Filter for Virtual Rotor Frequency Feedback: An additional low-pass filter can be introduced to process the PLL frequency ω_r (virtual rotor frequency) before it is used in the governor feedback loop. The low-pass filter is required to maintain stability in case of unusual tuning of the control scheme with very high damper winding constant, resulting in a high proportional gain $K_{\mathrm{pll,p}}$ of the PLL block. Accordingly, (25) is changed to

$$i_{\mathrm{g,d}} = \frac{P_{\mathrm{set}} - K_g(G_{\mathrm{lp}}(s)\omega_r - \omega_{\mathrm{set}})}{c_p V_N}. \tag{30}$$

A second-order low-pass filter with $\omega_0 = 0.5 \cdot \omega_N$ and a damping of $d = 0.7$ works well in most cases.

3) Active Damping With Virtual Resistor: If it is required to operate the converter also in stand-alone (islanded) conditions or for black-start, the control scheme needs a virtual termination resistor for stabilization in case there is no load connected to the system. An active damping scheme based on virtual resistor damping is implemented in d- and q-directions

$$i_{\mathrm{ad,d}} = G_{\mathrm{hp}}(s)\frac{1}{R_{\mathrm{ad}}}V_{\mathrm{p,d}} \tag{31}$$

$$i_{\mathrm{ad,q}} = G_{\mathrm{hp}}(s)\frac{1}{R_{\mathrm{ad}}}V_{\mathrm{p,q}}. \tag{32}$$

A second-order high-pass filter with $\omega_0 = 0.2 \cdot \omega_N$ and $d = 0.7$ is used to restrict the impact of the virtual resistor to high frequency harmonics exclusively.

The final current references are given with

$$i_d{}^* = i_{\mathrm{r,d}} + i_{\mathrm{v,d}} + i_{\mathrm{ad,d}} \tag{33}$$

$$i_q{}^* = i_{\mathrm{r,q}} + i_{\mathrm{v,q}} + i_{\mathrm{ad,q}}. \tag{34}$$

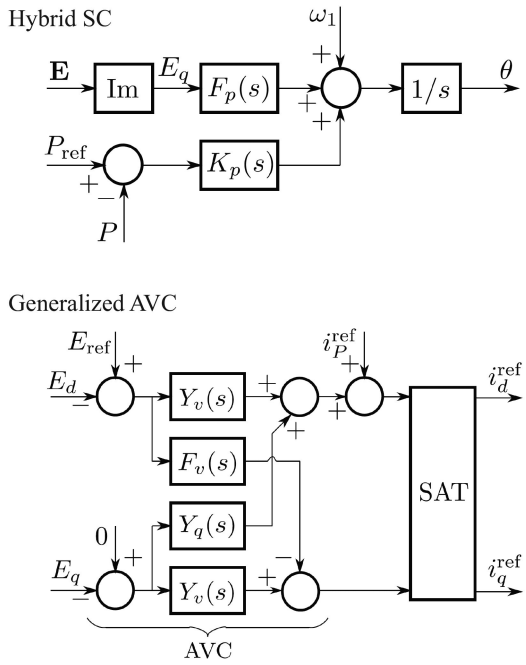

Fig. 5. Generic PLL-based grid-forming control structure consisting of a hybrid synchronization controller (SC) and a generalized ac-bus-voltage controller (AVC) [38].

TABLE I
MAPPING OF TRANSFER FUNCTIONS TO GENERIC GRID-FORMING CONTROL STRUCTURE

Generalized TF	GFVCC TF
$K_p(s)$	0
$F_p(s)$	$K_{\mathrm{pll,p}} + \frac{K_{\mathrm{pll,i}}}{s}$
$Y_v(s)$	$Y_{\mathrm{v,dd}}(s) + G_{\mathrm{hp}}(s)\frac{1}{R_{\mathrm{ad}}}$
$F_v(s)$	$-Y_{\mathrm{v,qd}}(s) = Y_{\mathrm{v,dq}}(s)$
$Y_q(s)$	$Y_{\mathrm{v,dq}}(s)$

IV. Generic PLL-Based Grid-Forming Control Structure

In [38], the structure of a generic PLL-based grid-forming controller has been presented. GFVCC is a further variant of such control schemes and it fits into the generic framework. The generalized control framework is based on a hybrid synchronization controller (SC) and a generalized ac-bus-voltage controller (AVC) according to Fig. 5. The variables are defined as $\mathbf{E} = E_d + jE_q$ and correspond to the variables used in GFVCC with $E_d = V_{\mathrm{p,d}}$, $E_q = V_{\mathrm{p,q}}$ and $E_{\mathrm{ref}} = V_v$. GFVCC can be mapped to the generalized structure by selecting the transfer functions according to Table I.

The main difference compared to the controllers proposed in [38] is that with GFVCC, the generalized AVC becomes symmetric and is related to a physical model of the virtual stator impedance. Furthermore, the hybrid SC parameters fall back to a standard PLL implementation without any further modifications.

V. Implementation

A. Simulation Setup

The control scheme has been implemented and tested in MATLAB/Simulink simulation environment.

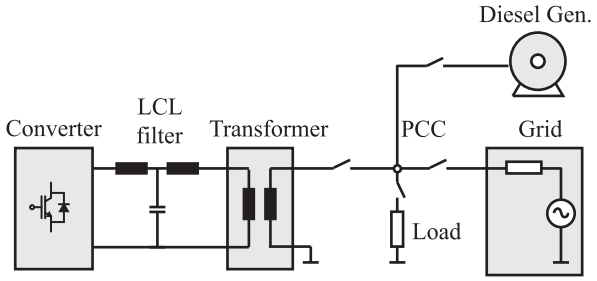

Fig. 6. Schematic diagram of the simulated setup.

TABLE II
DIESEL GENERATOR PARAMETERS

Description	Label	Value
Generator nominal power	$P_{\mathrm{N,dg}}$	250 kW
Generator reactances	X_d	2.98 p.u.
	$X_{\mathrm{d,tr}}$	0.26 p.u.
	$X_{\mathrm{d,str}}$	0.18 p.u.
	X_q	1.32 p.u.
	$X_{\mathrm{q,str}}$	0.22 p.u.
	X_l	0.12 p.u.
Short circuit time constants	$T_{\mathrm{d,tr}}$	0.362 s
	$T_{\mathrm{d,str}}$	0.008 s
	$T_{\mathrm{q,str}}$	0.017 s
Stator resistance	R_s	0.008 p.u.
Inertia	H	1 s
Frequency droop	$K_{\mathrm{g,dg}}$	33.3 p.u.

The electrical part of the simulation is built with SimPowerSystems Library blocks. The converter is connected with an *LCL*-filter and a transformer to the grid. The transformer model is linear and it is configured as Dyn11, i.e., the windings are connected in delta at the converter side and in star with grounded star-point at the PCC side. The PLL is fed with the PCC voltage after the transformer instead of using the capacitor voltage, what has only a minor impact on the overall control performance. The simulation environment is capable of emulating load steps as well as faults and islanding events. Besides operating with a stiff grid (a voltage source behind a configurable grid impedance), the system can also be connected to a model of a diesel generator with speed governor control [cf., Fig. 6].

The nominal power of the converter is 100 kW and the nominal power of the diesel generator is 250 kW. The *LCL* filter parameters, the transformer data and the tuning parameters of the control scheme are given in Table III. Parameters of the diesel generator and engine are summarized in Table II. A PI-type speed controller and an IEEE type 1 synchronous machine voltage regulator combined to an exciter are used.

B. Control Implementation and Tuning Approach

A classical current control scheme in synchronous reference frame (*dq*-coordinates) has been used as a starting point (cf., Fig. 7). The control algorithm was implemented as a sampled subsystem with a sampling frequency of 14 kHz, emulating double update mode of a converter with a switching frequency of 7 kHz. Sample delays have been introduced to account for the typical delays occurring in a discrete implementation on a control platform. The virtual admittance was transformed to discrete form using Tustin's method (cf., [39]). In order to speed up the simulation, implementation of the modulator and power electronic switching stage have been avoided. Only the typical delay of the modulation stage was included and the output of the sampled subsystem directly drives controlled voltage sources.

TABLE III
CONTROL SCHEME PARAMETERS

Description	Label	Value
Converter nominal power	P_N	100 kW
Nominal bus voltage	V_N	400 V
Nominal angular frequency	ω_N	$2\pi 50\,\mathrm{rad/s}$
Converter side inductance	L_{fc}	0.04 p.u.
Filter capacitance	C_f	0.1 p.u.
Grid side inductance	L_{fg}	0.02 p.u.
Transformer leakage inductance	$L_{\mathrm{t}\sigma}$	0.04 p.u.
Droop constant	K_g	33.3 p.u.
Voltage droop constant	K_{Vd}	25 p.u.
Virtual inertia	M	$624\,\mathrm{Ws}^2$, ($H = 1$ s)
Damper winding constant	K_f	46.3 p.u.
Virtual inductance	L_v	0.18 p.u.
Virtual resistance	R_v	0.045 p.u.
Active damping resistor	R_{ad}	0.66 p.u.
Prop. gain current control	k_p	0.2 p.u.
Integr. gain current control	k_i	4.0 p.u.

Two PI-type control blocks with antiwindup scheme and feedforward of the measured capacitor voltage are used for the current control. The current references are saturated with an angle preserving scheme, i.e., the magnitude of the current vector is limited to the maximum value. The output of the current control blocks, i.e., the converter reference voltage vector, is again saturated with an angle preserving scheme. This method limits the maximum output voltage effectively. Furthermore, the PCC voltage is supported with the AVR according to the voltage droop curve as long as the current limit of the converter is not reached. Although closed-loop voltage magnitude control probably would surpass the voltage control performance, it is not foreseen in the proposed current control-based concept.

The gains of the current control blocks are tuned with a standard approach considering the *LCL* filter resonance (cf., [40]). The transformer leakage inductance and the grid inductance are accounted to the grid side inductance L_{fg} of the *LCL* filter. If a wide range of different grid strengths needs to be covered in a grid connected application, the current control gains are tuned for the highest expected grid impedance.

The tuning of the remaining control parameters is based on the idea to reproduce the output characteristics of a synchronous generator. The PLL gains are tuned according to the VSM equivalency rules defined in (13) and (14). The virtual inertia M is related to the inertia constant H, the nominal apparent power S_N and the nominal angular frequency ω_N of a synchronous generator with

$$M = 2H\frac{S_N}{\omega_N}. \tag{35}$$

The inertia constant of a real generator typically is in the range of $H = 1\ldots10$ s and it is suggested to tune M accordingly. The damper winding constant is related to the damping factor D of

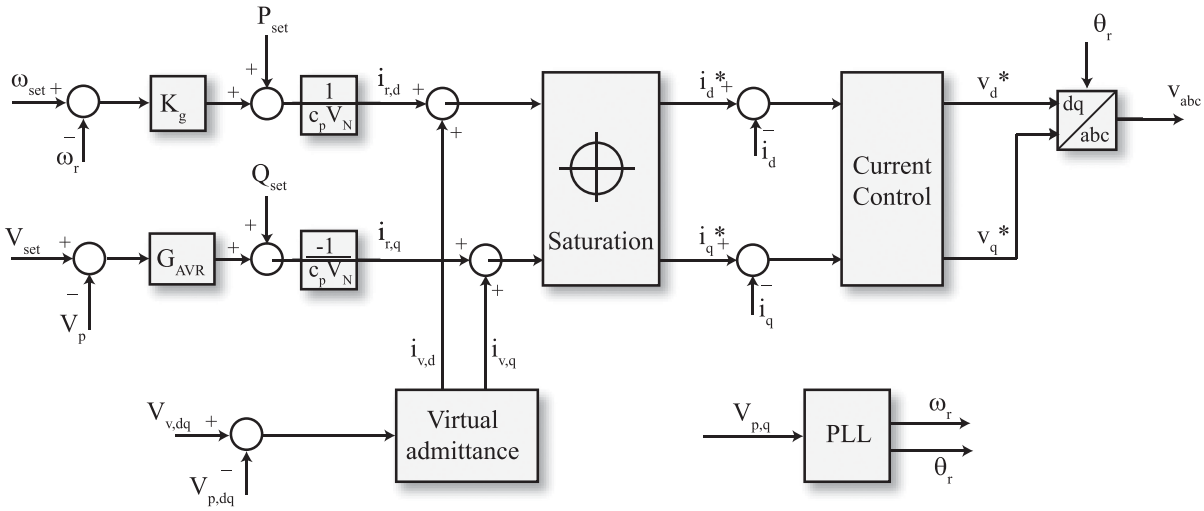

Fig. 7. Control block diagram of GFVCC.

the PLL with

$$K_f = 2DV_p\sqrt{c_p\frac{M}{X_v}}. \tag{36}$$

A real generator typically achieves only weak damping with the damper winding and is prone to low frequency rotor speed oscillations. These oscillations can be reduced by selecting the damping factor in a higher range of $D = 0.5\ldots1$.

The proposed tuning approach of VSM equivalency results in a PLL with low bandwidth $f_{0,\mathrm{pll}} < 5$ Hz which is suitable for compatibility with weak grids (cf., [41]). The usage of further filtering stages for the PLL is not encouraged as they would change the emulated inertia and are not necessarily required with a low bandwidth PLL.

The stator reactance of a typical synchronous generator is in the range of $X_s = 0.1\ldots1$ p.u. and it is suggested to select the virtual reactance X_v in a similar range. The virtual resistance is selected in the range of $R_v = 0.05\ldots0.25 \cdot X_v$ for improved damping of high frequency resonances.

Tuning of the frequency and voltage droop curves is typically related to the application and needs to be coordinated among the units in the grid. Typically, values in the range of $K_g = 20\ldots50$ p.u. and $K_{\mathrm{Vu}} = 20\ldots50$ p.u. are chosen.

VI. Simulation Results

In the following, simulation results will show the basic performance of GFVCC. Typical scenarios are tested and the results are being discussed.

A. Response to Load Step for Grid-Connected Operation

The response of the converter to a load step while it is connected to a strong grid with a short circuit ratio (SCR) of 20 is shown in Fig. 8. After $t = 0.8$ s, a load of 1 p.u. is connected at the PCC. The converter reacts with a transient injection of active power. The remaining converter current after $t = 0.9$ s is due to increased injection of reactive power by the AVR to support the voltage at the PCC. The low frequency power oscillation is well damped due to the damper winding emulation. The current response is immediate with almost no delay. There is a short current spike coming from the ac capacitors in the *LCL* filter stage when the load is connected to the system. The current spike does not propagate to the converter side currents i_c and is not critical for the inverter power electronics.

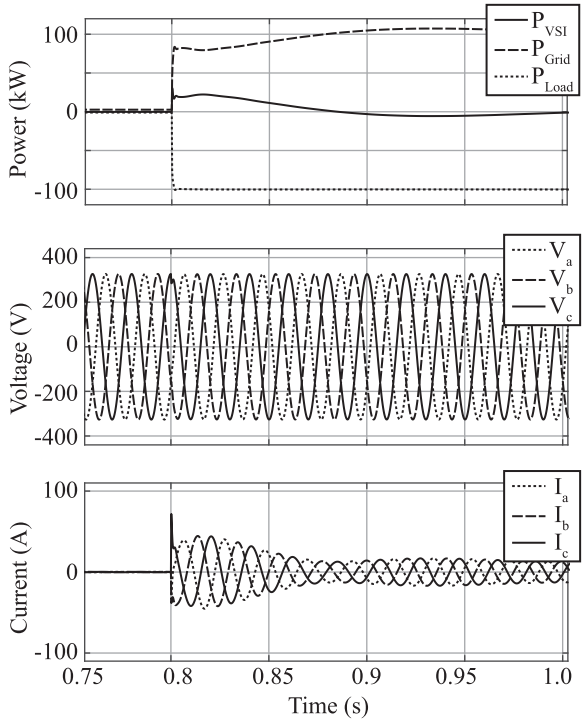

Fig. 8. Output power, PCC voltage, and current waveforms during a load step while connected to a stiff grid.

B. Power Reference Tracking in Weak and Strong Grid

The active power setpoints are impressed with the virtual current source, i.e., the additional current set-points i_r given

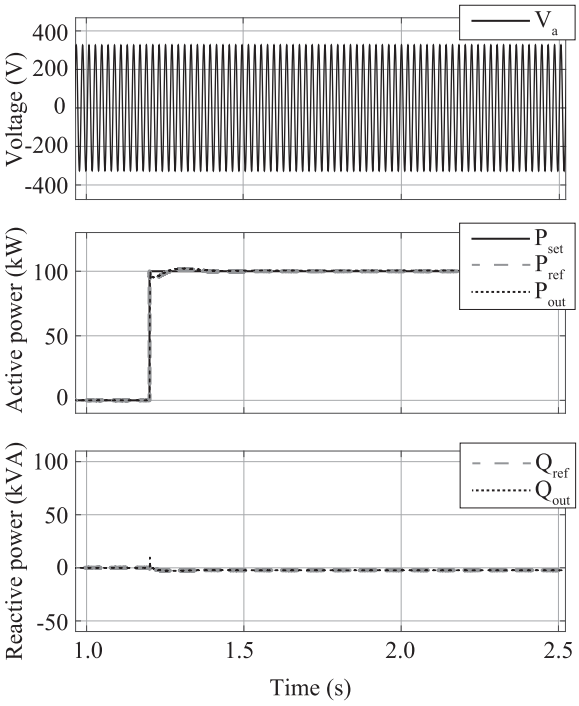

Fig. 9. Tracking of the power setpoint P_{set} in a strong grid (SCR=100).

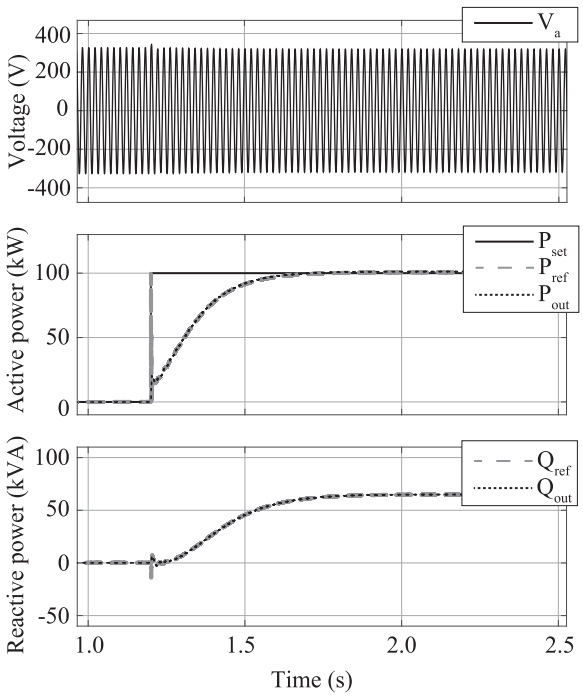

Fig. 10. Tracking of the power setpoint P_{set} in a weak grid (SCR=1.05).

to the controller. As the emulated spinning wheel always aligns with the grid angle in the steady state, there is zero active power injected by the spinning wheel in the steady state and the power is uniquely controlled by the virtual current source.

The strength of the grid has been adapted by changing the grid impedance $Z_g = R_g + jX_g$. The reactance of the grid impedance was set to $X_g = 0.01$ p.u. for the very strong grid (SCR=100) and to $X_g = 0.95$ p.u. for the weak grid (SCR=1.05). The grid impedance includes a small series resistance of $R_g = 0.01 \cdot X_g$.

The simulation results for active power setpoint tracking in a very strong grid (SCR=100) are shown in Fig. 9. The actual power reference P_{ref} for plotting is calculated with the final current references given to the controller and the PCC voltage. The actual output power P_{out} follows the reference accurately. The controller injects negligible reactive power because the bus voltage is very stable. The impact of the emulated spinning wheel is not pronounced and the power setpoint tracking performance is similar as with VCC only. The overshoot of the response can be adjusted with the damping coefficient K_f.

The simulation results for setpoint tracking in a weak grid (SCR=1.05) are shown in Fig. 10. The transient behavior of the spinning wheel leads to a smoothing effect which is more pronounced for weak grids than for strong grids. It slows down the power reference (dashed grey line) because it transiently absorbs the injected power of the virtual current source, i.e., the total active power reference rise-time is adapted to the absorption capability of the weak grid. Furthermore, the control scheme injects a significant amount of reactive power. One of the main issues regarding the performance of VCC in weak grids is the missing injection of appropriate amount of reactive power to stabilize the PCC voltage amplitude. Consequently, the PCC voltage can collapse when injecting high power. With GFVCC, this problem is solved because the emulated synchronous condenser together with the AVR provide enough reactive power to stabilize the PCC voltage. This important feature improves the performance of GFVCC in weak grids significantly, similar as with VSM control.

It is important to note that the control parameters have not been changed for the two cases despite the very different SCR of the grid. The rise time of the response is not directly determined by the current controller gains but by the total current reference itself which is adapted by the internal model, i.e., the emulated spinning wheel, and its interaction with the grid. Consequently, the rise-time and overshoot can be changed by adapting the virtual admittance Y_v, the emulated inertia M and damper winding constant K_f. Emulating a synchronous condenser with a lower nominal power, which is achieved by reducing the gain of the virtual admittance Y_v, will reduce the impact of the spinning wheel and the control performance will converge toward the performance of standard VCC.

C. Inertial Response

The injection of an appropriate amount of inertial power has been tested by simulating a frequency ramp with the grid. The speed governor has been deactivated in order to isolate the inertial response of the spinning wheel. According to the swing equation, the injected power is given as $P_{\text{out}} = -M \cdot d\omega_r/dt$. Two frequency ramps with different steepness have been simulated and the inverter output is compared to the expected output power. For both cases, the actual power output is equal to the expected inertial response (cf., Fig. 11).

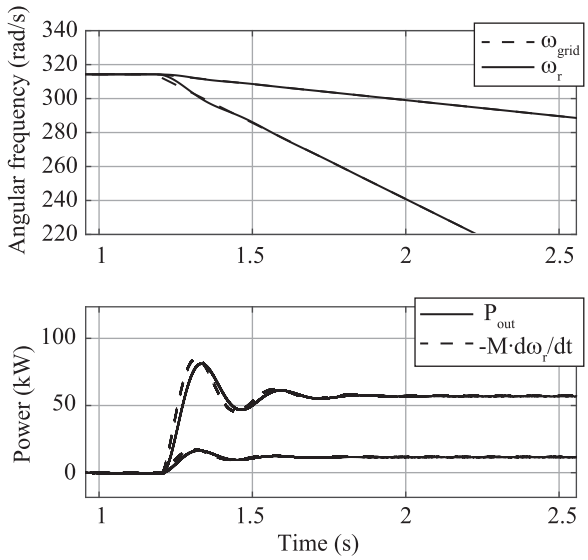

Fig. 11. Injection of inertial power in reaction to two grid frequency ramps with $df/dt = 3$ Hz/s and $df/dt = 15$ Hz/s.

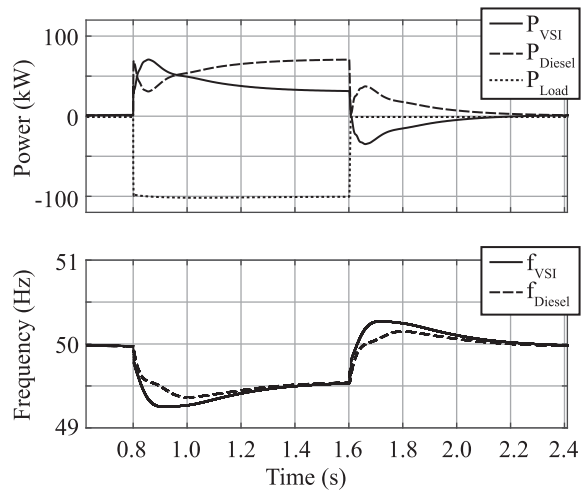

Fig. 12. Output power and rotor frequency evolution during a load step while connected to a diesel generator.

D. Converter Connected to Diesel Generator

If the converter is connected to a diesel generator instead of to a stiff grid, the frequency will also change during load steps. The simulation results for a load step of 1 p.u. are depicted in Fig. 12. In this case, the grid is disconnected. The load is shared immediately between the converter and the diesel generator after load connection. Subsequently, the converter increases the output power slightly for a short time interval to support the load, because the diesel generator governor control reacts with a time delay. After a while, the output power of both units converge to the values given by the droop curves

Again, the inertial response of GFVCC can be tested if its droop control loop is deactivated. In this case, the grid frequency is stabilized by the diesel generator only and the converter injects transient power as long as the frequency is changing. According to the swing equation, the injected power is given as

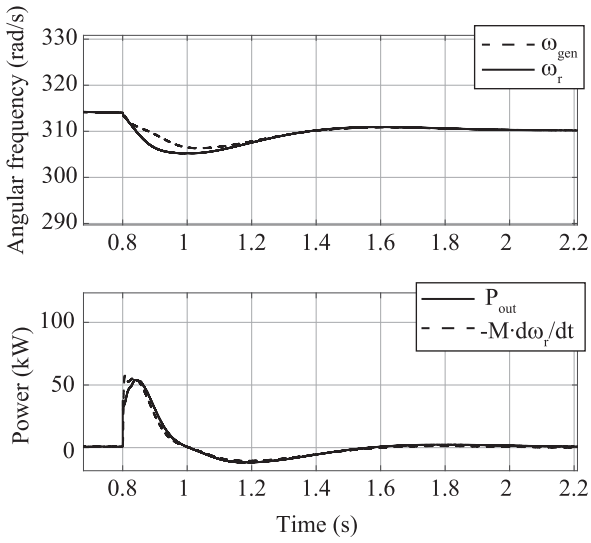

Fig. 13. Inertial response of GFVCC when connected to a diesel generator.

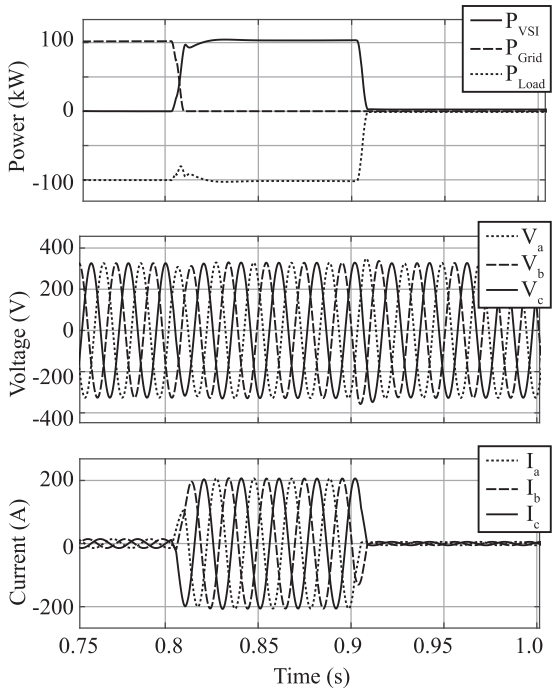

Fig. 14. Converter behavior during an unplanned islanding event and a subsequent load shedding event.

$P_{\text{out}} = -M \cdot d\omega_r/dt$. The simulation result is shown in Fig. 13. The power output of the converter matches the expected response accurately.

E. Islanding and Stand-Alone Operation

The control scheme is able to operate without any grid connection at all. An unplanned loss of grid connection at $t = 0.8$ s is simulated and shown in Fig. 14. The converter immediately supplies the load of 1 p.u. connected at the PCC. The voltage waveforms are disturbed only slightly. After another 100 ms, the load is disconnected. The converter continues to generate

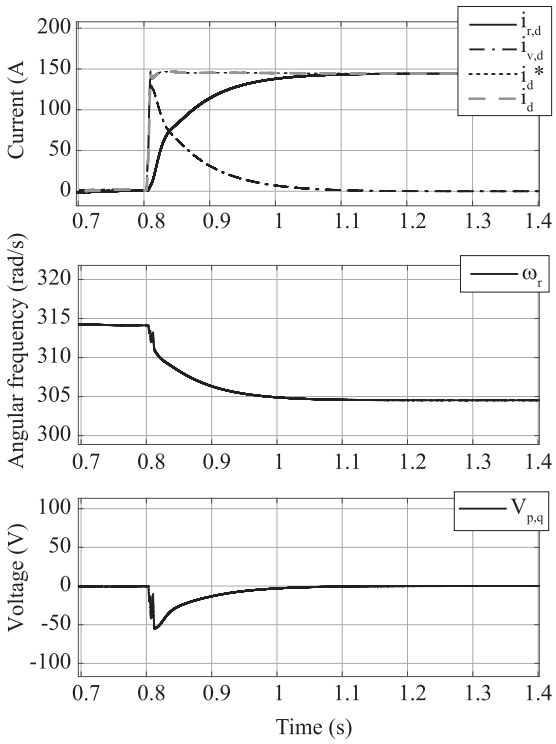

Fig. 15. Detailed view of individual components of the current reference, the internal frequency and the q-component of the PCC voltage during a load step in stand-alone operation.

the three-phase ac voltages, no instability is observed. The bus voltage after the load shedding event shows a slight overshoot which could be reduced with a smaller virtual reactance X_v or faster AVR.

To explain the control behavior in islanded operation, the individual components of the current reference have to be analyzed. The system is only stable with the droop control (speed governor) activated. Otherwise, the frequency ω_r will decay to zero according to $d\omega_r/dt = -P_{\text{out}}/M$. At the very first moment when a load is connected to the stand-alone system or if an unplanned islanding event occurs, the voltage angle at the PCC with respect to the internal angle of the spinning wheel (PLL) will shift until the balance of $P_{\text{load}} = P_{\text{out}} = c_p V_{\text{p,d}} i_{\text{v,d}} = -c_p V_{\text{p,d}} V_{\text{p,q}}/X_v$ is established. $V_{\text{p,q}}$ is not zero at the beginning, however, the integrator action of the PLL will try to nullify $V_{\text{p,q}}$ by reducing the frequency ω_r. Consequently, the droop control loop (governor) will start to increase $i_{\text{r,d}}$ until it has completely replaced $i_{\text{v,d}}$ and the frequency balances at a new steady-state given by the droop curve. At this point $V_{\text{p,q}}$ and $i_{\text{v,d}}$ become zero again, the complete output power is injected by the virtual current source. The individual current components $i_{\text{v,d}}$ and $i_{\text{r,d}}$, and the total current reference $i_d{}^*$ are shown in Fig. 15 during a load step in stand-alone (islanded) operation.

F. Black-Start

The control scheme can be configured to energize a dead bus. The bus voltage can be ramped up by increasing the value of V_v slowly and the control scheme will impress the voltage over the virtual admittance and the AVR. For the following tests, the circuit breaker has been closed from the beginning. The inrush current of the transformer is minimized due to the slow increase of the bus voltage magnitude.

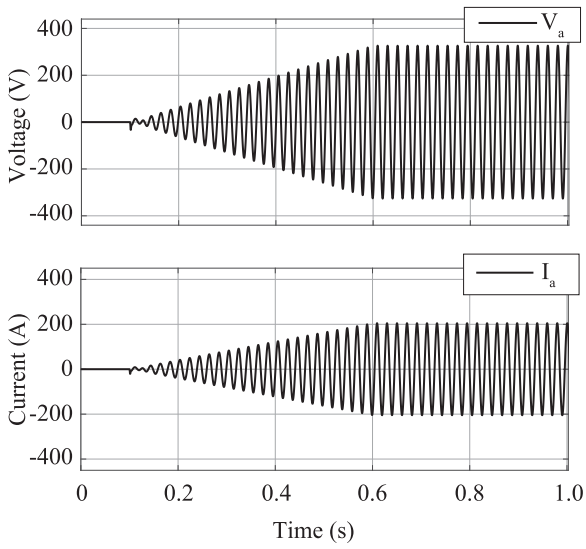

Fig. 16. Bus voltages and currents during a black-start process with resistive load.

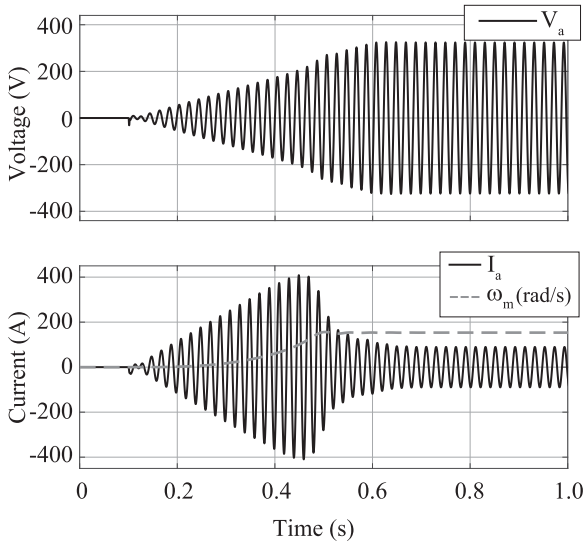

Fig. 17. Bus voltages and currents during a black-start process with an induction machine connected to the bus.

The waveforms for a black-start process with a resistive load bank with a nominal power of 1 p.u. connected to the bus are depicted in Fig. 16. The waveforms are clean and the bus voltage is ramped up smoothly.

A more difficult case is a black-start with a high share of induction machines (IM) connected to the bus, because they have a high starting current. An IM with a nominal power of 0.37 p.u. and quadratic torque-speed load has been connected to the bus. The simulated waveforms for this case are shown in Fig. 17, where ω_m denotes the angular frequency of the rotor. The peak starting current should be below the current limitation of the

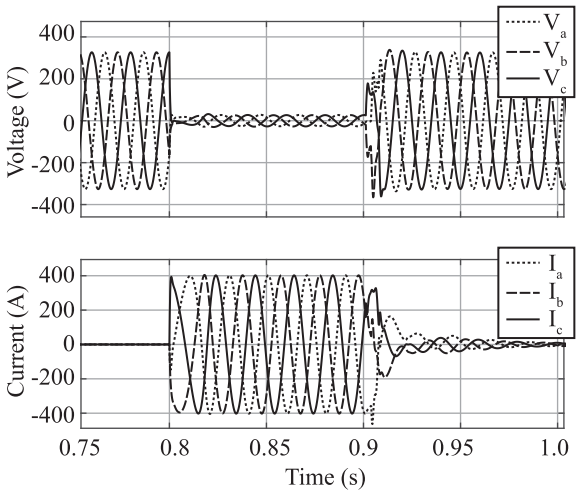

Fig. 18. Voltage and current waveforms for a three-phase fault at the PCC.

converter. Ramping up the voltage magnitude with a reduced slope will lower the starting current because the effect is similar to a soft-starter for the machine.

G. Fault Behavior

Fault handling is the most difficult task with respect to converter control, especially if the converter is operated with a voltage-based VSG control scheme. Typically, additional control loops are required for current limitation and after clearing of the fault, resynchronization issues are common [31]. With GFVCC, the fault handling capability is improved. Due to the inherent current control, the fault current can be limited to a given value to avoid damaging of semiconductors.

The reaction of the converter to a bolted three-phase fault while connected to the grid (SCR=20) has been simulated and is shown in Fig. 18. During the fault, the currents are limited to 2 p.u. and reactive power is injected. A simple fault detection logic has been implemented. The PLL frequency is frozen as soon as the bus voltage magnitude falls below 0.3 p.u. and released again when it rises above the threshold. The converter resynchronizes immediately after the fault is cleared and no severe power oscillations can be observed.

The waveforms for a single phase to ground fault are depicted in Fig. 19. The converter currents $I_{\mathrm{a-c}}$ are highly distorted due to the asymmetric condition of the fault and the active current limitation. The controller manages to cap the currents at 2 p.u. approximately. The currents after the transformer at the PCC $I_{\mathrm{p,a-c}}$ have significant negative and zero sequence components. The zero sequence component is not controlled with the converter as it is blocked by the transformer.

VII. Experimental Results

The control scheme has been implemented on a 25-kW inverter unit. The inverter implements a two-level topology using SiC-MOSFETs to support an increased switching frequency of 30 kHz and a high control bandwidth. The digital control

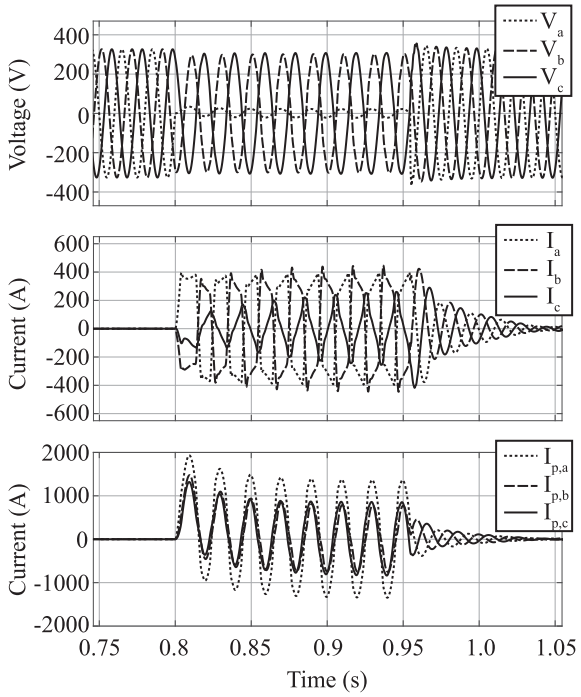

Fig. 19. Waveforms for a single-phase to ground fault at the PCC.

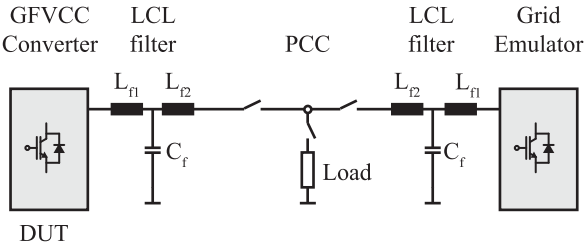

Fig. 20. Schematic diagram of the experimental setup.

platform is based on a 32 bit Arm Cortex-M4F from Infineon (XMC4800E196K2048).

A second, identical inverter unit has been used as a grid emulator. The two inverter units are coupled on the ac side over their individual *LCL* output filter stages and a resistive load can be attached at the PCC (cf., Fig. 20). The two inverter units are fed with two isolated four quadrant power supplies which are connected to their dc-links. Load steps, islanding events and frequency sweeps can be performed with the experimental setup.

The key converter properties and the tuning of the control scheme parameters are summarized in Table IV.

A. Grid-Connected Operation

In a first test, injection of inertial power in response to a load step at the PCC is evaluated. The second converter is operated as a grid emulator with a fixed frequency and a virtual output impedance of 0.15 p.u. to emulate a rather weak grid. A resistive load of 25 kW is connected at $t = 0$ s (cf., Fig. 21). As expected, the converter operating with GFVCC injects active power for a short amount of time to support the weak grid with transient power. The distribution of power at the moment of connection

TABLE IV
CONVERTER PROPERTIES AND CONTROL SCHEME PARAMETERS

Description	Label	Value
Converter nominal power	P_N	25 kW
Switching frequency	f_{sw}	30 kHz
Nominal bus voltage	V_N	208 V
Nominal angular frequency	ω_N	$2\pi 60\,\mathrm{rad/s}$
Converter side inductance	L_{f1}	$100\,\mu$H
Filter capacitance	C_f	$66\,\mu$F
Grid side inductance	L_{f2}	$5\,\mu$H
Control sampling frequency	f_s	15 kHz
Droop constant	K_g	30 p.u.
Voltage droop constant	K_{Vs}	1.7 p.u.
Virtual inertia	M	$1070\,\mathrm{Ws}^2$
Damper winding constant	K_f	404 p.u.
Virtual inductance	L_v	0.15 p.u.
Virtual resistance	R_v	0.015 p.u.
Active damping resistor	R_{ad}	0.2 p.u.
Prop. gain current control	k_p	0.12 p.u.
Integr. gain current control	k_i	0.9 p.u.

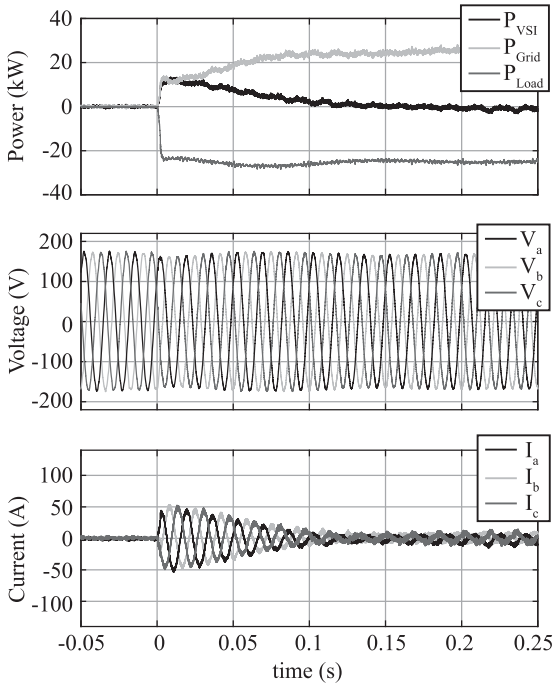

Fig. 21. Output power, PCC voltage, and current waveforms during a load step while connected to the grid emulator.

of the resistive load is one to one because the emulated output impedances of the two converters are equal. After a few cycles, the injected active power decays to zero and a low amount of reactive power is injected to support the PCC voltage amplitude.

The tracking of a change of the power setpoint while connected to the grid emulator is shown in Fig. 22. The total power injected to the grid is changed rather slowly although there is a step change in the setpoint, what can be explained with the effect of the emulated spinning wheel transiently absorbing part of the power set-point change. The setpoint is tracked accurately in steady state. The experimental results are similar to the results obtained with the simulation for a weak grid but with a reduced overshoot.

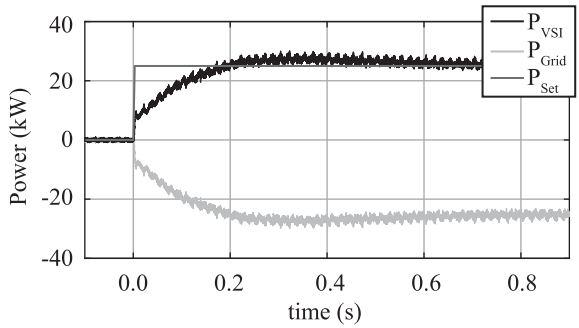

Fig. 22. Tracking of active power setpoint P_{set} while connected to the grid emulator.

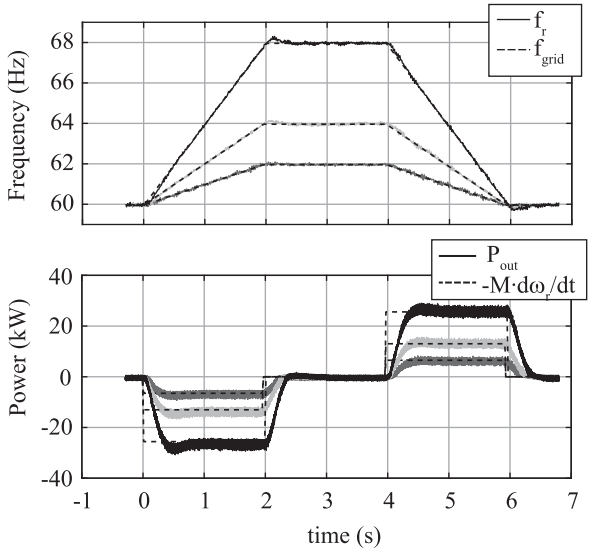

Fig. 23. Injection of inertial power in reaction to grid frequency ramps with $df/dt = 1$ Hz/s, $df/dt = 2$ Hz/s, and $df/dt = 4$ Hz/s.

B. Inertial Response

The accurate emulation of virtual inertia is tested with the response to frequency ramps created with the grid emulator. Positive and negative grid frequency ramps with different slopes are emulated and the injected active power of the converter operated with GFVCC is recorded (cf., Fig. 23). For this test, the frequency droop feedback loop has been disabled to evaluate the injected power related to virtual inertia only. The solid lines represent the measured injected power, whereas the dashed lines show the power calculated with $P_{\mathrm{out}} = -M \cdot d\omega_g/dt$ and the grid angular frequency derivative. The injected power follows the theoretical inertial power accurately without significant ringing or overshoot.

C. Islanding and Stand-Alone Operation

A grid-forming control scheme should be capable to operate in stand-alone conditions and to survive unintended islanding events.

At the beginning of this test, the converter is connected to the grid emulator and a resistive load is connected at the PCC. In steady state, the load is supplied by the grid emulator only as

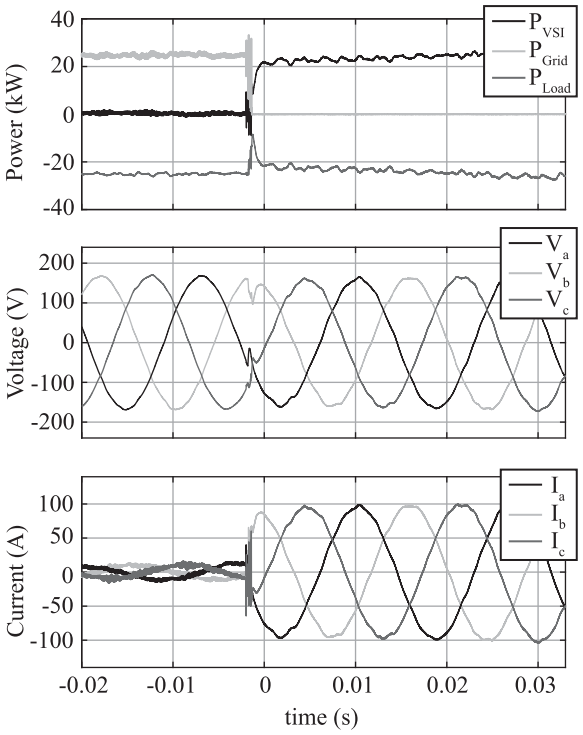

Fig. 24. Converter behavior during an unplanned islanding event.

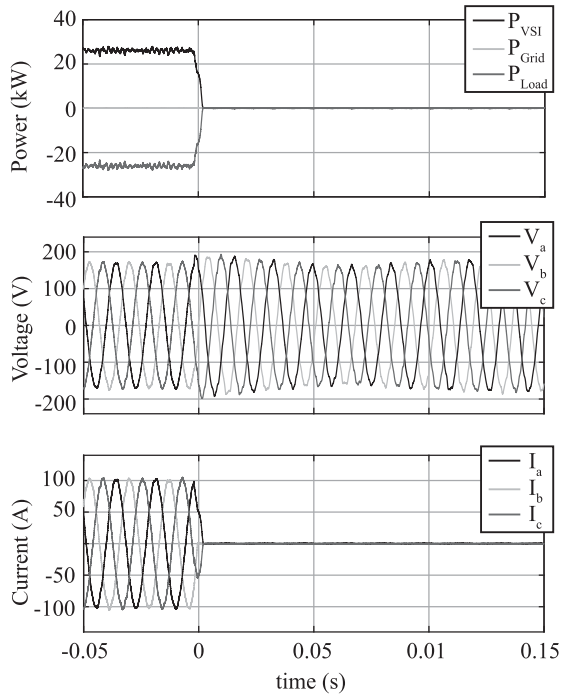

Fig. 25. Converter behavior during a load shedding event.

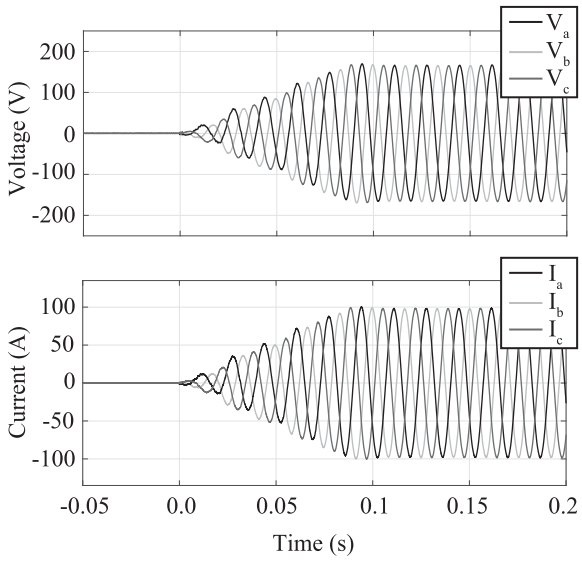

Fig. 26. Bus voltages during a black-start process with the converter.

the grid frequency is fixed at the nominal frequency and consequently, there is no active current reference from the frequency droop feedback loop. At $t = 0$ s, the grid emulator is suddenly disconnected from the setup (cf., Fig. 24). A voltage dip can be observed at the PCC, but within only 1 ms, the bus voltage is reestablished and the load is fed from the GFVCC converter. The voltage amplitude has dropped slightly, but the system is stable and continues to operate without grid connection. The grid frequency will be reduced slightly according to the frequency droop curve.

In a second test, the response of the converter in case of a load shedding event is evaluated. From a stability point of view, this condition is difficult to handle because there is very little passive damping in the system without any load and there is the risk of PCC voltage overshoot when the load is disconnected. At the beginning of the test, the converter is operated in islanded conditions without any grid connection and it supplies a resistive load (cf., Fig. 25). Subsequently, the resistive load is disconnected. The increase of the voltage magnitude at the PCC right after the load shedding event is 10%. The voltage amplitude is reduced to its nominal value after a few line cycles. The control system is stable in stand-alone operation without any resistive load connected to the PCC. The performance of the voltage amplitude control could be improved with a higher gain of the AVR and a smaller virtual reactance X_v.

D. Black-Start

Finally, a black-start process is performed with the converter. For this test, the grid emulator is disconnected from the system and a 1 p.u. resistive load is connected to the PCC. The bus voltage is ramped up by increasing slowly the value of V_v. The PCC voltage increases smoothly and the converter energizes the bus without any stability issues (cf., Fig. 26).

VIII. Conclusion

Grid-forming control becomes more and more important in various applications, such as microgrids, grid-connected BESS, railway interties, PV, and HVDC. TSOs and DSOs are discussing if standards for converter-connected energy resources should be changed in such a way that grid support becomes mandatory.

With this background, it is important that existing grid-forming control methods are simplified and improved.

A control scheme designated as grid-forming vector current control has been proposed in this article. It has been shown that standard vector current control can be adapted with minor modifications to emulate the behavior of a virtual synchronous condenser that is connected in parallel with a virtual current source. The control scheme offers reduced complexity and can easily be implemented on existing converter control platforms. It has inherent current limitation and it is capable to operate without any grid connection, i.e., it is stable also in stand-alone operation.

Simulation results and experimental results are provided and discussed to demonstrate the control performance under various scenarios such as load steps, parallel operation with a diesel generator, islanding, and grid faults. Basic control performance has been proven for all scenarios.

Open points such as a detailed comparison with traditional VSG implementations and a comparison with voltage reference-based methods should be investigated in the future.

REFERENCES

[1] M. Ndreko, S. Rüberg, and W. Winter, "Grid forming control for stable power systems with up to 100 % inverter based generation: A paradigm scenario using the IEEE 118-bus system," in *Proc. 17th Int. Workshop Large-Scale Integration Wind Power Power Syst. Transmiss. Netw. Offshore Wind Power Plants*, 2018, pp. 16–18.

[2] F. Milano, F. Dörfler, G. Hug, D. J. Hill, and G. Verbic, "Foundations and challenges of low-inertia systems (invited paper)," in *Proc. Power Syst. Comput. Conf.*, 2018, pp. 1–25.

[3] J. Rocabert, A. Luna, F. Blaabjerg, and P. Rodriguez, "Control of power converters in AC microgrids," *IEEE Trans. Power Electron.*, vol. 27, no. 11, pp. 4734–4749, Nov. 2012.

[4] Y. Sun, X. Hou, J. Yang, H. Han, M. Su, and J. M. Guerrero, "New perspectives on droop control in AC microgrid," *IEEE Trans. Ind. Electron.*, vol. 64, no. 7, pp. 5741–5745, Jul. 2017.

[5] S. d'Arco and J. A. Suul, "Virtual synchronous machines - classification of implementations and analysis of equivalence to droop controllers for microgrids," in *Proc. IEEE Grenoble Conf.*, 2013, pp. 1–7.

[6] H. Bevrani, T. Ise, and Y. Miura, "Virtual synchronous generators: A survey and new perspectives," *Int. J. Elect. Power Energy Syst.*, vol. 54, pp. 244–254, 2014.

[7] H. J. Künisch, K. G. Krämer, and H. Dominik, "Battery energy storage another option for load-frequency-control and instantaneous reserve," *IEEE Trans. Energy Convers.*, vol. EC-1, no. 3, pp. 41–46, Sep. 1986.

[8] M. C. Chandorkar, D. M. Divan, and R. Adapa, "Control of parallel connected inverters in standalone AC supply systems," *IEEE Trans. Ind. Appl.*, vol. 29, no. 1, pp. 136–143, Jan. 1993.

[9] A. Tuladhar, H. Jin, T. Unger, and K. Mauch, "Parallel operation of single phase inverter modules with no control interconnections," in *Proc. Appl. Power Electron. Conf.*, 1997, vol. 1, pp. 94–100.

[10] A. Engler, "Control of parallel operating battery inverters," in *Proc. Photovolt. Hybrid Power Syst. Conf.*, 2000, pp. 1–4.

[11] A. Engler and N. Soultanis, "Droop control in LV-grids," in *Proc. Int. Conf. Future Power Syst.*, 2005, pp. 1–6.

[12] S. J. Chiang, C. Y. Yen, and K. T. Chang, "A multimodule parallelable series-connected PWM voltage regulator," *IEEE Trans. Ind. Electron.*, vol. 48, no. 3, pp. 506–516, Jun. 2001.

[13] J. M. Guerrero, L. G. de Vicuna, J. Matas, M. Castilla, and J. Miret, "Output impedance design of parallel-connected UPS inverters with wireless load-sharing control," *IEEE Trans. Ind. Electron.*, vol. 52, no. 4, pp. 1126–1135, Aug. 2005.

[14] J. M. Guerrero, J. Matas, L. Garcia De Vicunagarcia De Vicuna, M. Castilla, and J. Miret, "Wireless-control strategy for parallel operation of distributed-generation inverters," *IEEE Trans. Ind. Electron.*, vol. 53, no. 5, pp. 1461–1470, Oct. 2006.

[15] J. Liu, Y. Miura, and T. Ise, "Comparison of dynamic characteristics between virtual synchronous generator and droop control in inverter-based distributed generators," *IEEE Trans. Power Electron.*, vol. 31, no. 5, pp. 3600–3611, May 2016.

[16] H. Beck and R. Hesse, "Virtual synchronous machine," in *Proc. 9th Int. Conf. Elect. Power Qual. Utilisation*, 2007, pp. 1–6.

[17] J. Driesen and K. Visscher, "Virtual synchronous generators," in *Proc. IEEE Power Energy Soc. Gen. Meeting - Convers. Del. Elect. Energy 21st Century*, 2008, pp. 1–3.

[18] Y. P. Chen, R. Hesse, D. Turschner, and H.-P. Beck, "Comparison of methods for implementing virtual synchronous machine on inverters," in *Proc. Int. Conf. Renewable Energies Power Qual.*, 2012, pp. 414–424.

[19] Q. Zhong and G. Weiss, "Synchronverters: Inverters that mimic synchronous generators," *IEEE Trans. Ind. Electron.*, vol. 58, no. 4, pp. 1259–1267, Apr. 2011.

[20] V. Natarajan and G. Weiss, "Synchronverters with better stability due to virtual inductors, virtual capacitors, and anti-windup," *IEEE Trans. Ind. Electron.*, vol. 64, no. 7, pp. 5994–6004, Jul. 2017.

[21] L. Zhang, L. Harnefors, and H. P. Nee, "Power-synchronization control of grid-connected voltage-source converters," *IEEE Trans. Power Syst.*, vol. 25, no. 2, pp. 809–820, May 2010.

[22] A. Gonzalez-Cajigas, J. R. Perez, and E. Bueno, "Design and analysis of parallel-connected grid-forming virtual synchronous machines for island and grid-connected applications," *IEEE Trans. Power Electron.*, vol. 37, no. 5, pp. 5107–5121, May 2022.

[23] T. Loix, S. De Breucker, P. Vanassche, J. Van den Keybus, J. Driesen, and K. Visscher, "Layout and performance of the power electronic converter platform for the VSYNC project," in *Proc. IEEE Bucharest PowerTech*, 2009, pp. 1–8.

[24] D. Duckwitz and B. Fischer, "Modeling and design of df/dt -based inertia control for power converters," *IEEE Trans. Emerg. Sel. Top. Power Electron.*, vol. 5, no. 4, pp. 1553–1564, Dec. 2017.

[25] J. Fang, R. Zhang, H. Li, and Y. Tang, "Frequency derivative-based inertia enhancement by grid-connected power converters with a frequency-locked-loop," *IEEE Trans. Smart Grid*, vol. 10, no. 5, pp. 4918–4927, Sep. 2019.

[26] H. Alatrash, A. Mensah, E. Mark, G. Haddad, and J. Enslin, "Generator emulation controls for photovoltaic inverters," *IEEE Trans. Smart Grid*, vol. 3, no. 2, pp. 996–1011, Jun. 2012.

[27] M. P. N. van Wesenbeeck, S. W. H. de Haan, P. Varela, and K. Visscher, "Grid tied converter with virtual kinetic storage," in *Proc. IEEE Bucharest PowerTech*, 2009, pp. 1–7.

[28] P. Unruh, M. Nuschke, P. Strauss, and F. Welck, "Overview on grid-forming inverter control methods," *Energies*, vol. 13, no. 10, 2020, Art. no. 2589. [Online]. Available: https://www.mdpi.com/1996-1073/13/10/2589

[29] M. Zhang, X. Yuan, and J. Hu, "Inertia and primary frequency provisions of PLL-synchronized VSC HVDC when attached to islanded AC system," *IEEE Trans. Power Syst.*, vol. 33, no. 4, pp. 4179–4188, Jul. 2018.

[30] S. D'Arco, J. A. Suul, and O. B. Fosso, "Control system tuning and stability analysis of virtual synchronous machines," in *Proc. IEEE Energy Convers. Congr. Expo.*, 2013, pp. 2664–2671.

[31] J. Jongudomkarn, J. Liu, and T. Ise, "Comparison of current-limiting strategies of virtual synchronous generator control during fault ride-through," in *Proc. 10th IFAC Symp. Control Power Energy Syst.*, 2018, vol. 51, no. 28, pp. 256–261.

[32] H. Wu and X. Wang, "Design-oriented transient stability analysis of PLL-synchronized voltage-source converters," *IEEE Trans. Power Electron.*, vol. 35, no. 4, pp. 3573–3589, Apr. 2020.

[33] D. Duckwitz, "Performance of DF/DT-based inertia control during emergency islanding," in *Proc. 15th Wind Integration Workshop*, 2016, pp. 1–5.

[34] T. Soong and P. W. Lehn, "Evaluation of emerging modular multilevel converters for BESS applications," *IEEE Trans. Power Del.*, vol. 29, no. 5, pp. 2086–2094, Oct. 2014.

[35] O. D. Adeuyi, M. Cheah-Mane, J. Liang, and N. Jenkins, "Fast frequency response from offshore multiterminal VSC HVDC schemes," *IEEE Trans. Power Del.*, vol. 32, no. 6, pp. 2442–2452, Dec. 2017.

[36] H. Xie, L. Angquist, and H. P. Nee, "Design study of a converter interface interconnecting energy storage with the DC link of a statCom," *IEEE Trans. Power Del.*, vol. 26, no. 4, pp. 2676–2686, Oct. 2011.

[37] P. D. Judge and T. C. Green, "Modular multilevel converter with partially rated integrated energy storage suitable for frequency support and ancillary service provision," *IEEE Trans. Power Del.*, vol. 34, no. 1, pp. 208–219, Feb. 2019.

[38] L. Harnefors, M. Schweizer, J. Kukkola, M. Routimo, M. Hinkkanen, and X. Wang, "Generic PLL-based grid-forming control," *IEEE Trans. Power Electron.*, vol. 37, no. 2, pp. 1201–1204, Feb. 2022.
[39] M. Talha and I. A. Makda, "Frequency-domain modeling and Tustin discretization method based controlling of DC step-up chopper," in *Proc. 4th Int. Conf. Power Electron. Appl.*, 2019, pp. 1–5.
[40] E. Rodriguez-Diaz, F. D. Freijedo, J. C. Vasquez, and J. M. Guerrero, "Analysis and comparison of notch filter and capacitor voltage feedforward active damping techniques for LCL grid-connected converters," *IEEE Trans. Power Electron.*, vol. 34, no. 4, pp. 3958–3972, Apr. 2019.
[41] G. Wu *et al.*, "Parameter design oriented analysis of the current control stability of the weak-grid-tied VSC," *IEEE Trans. Power Del.*, vol. 36, no. 3, pp. 1458–1470, Jun. 2021.

Mario Schweizer (Member, IEEE) received the M.Sc. and Ph.D. degrees in electrical engineering from ETH Zurich, Zurich, Switzerland, in 2008 and 2012, respectively.

Since 2013, he has been with ABB Corporate Research, Zurich, Switzerland, where he is currently working as a Senior Principal Scientist with the Power Electronic Systems Group. He is, in addition, a Lecturer of power electronics and drives with the University of Applied Sciences and Arts Northwestern (FHNW) Switzerland, Windisch, Switzerland. His research interests include advanced converter topologies, converter control, and converter interaction in the future power grid, and microgrids.

Stefan Almér was born in Stockholm, Sweden. He received the M.Sc. degree in engineering physics and the Ph.D. degree in optimization and systems theory from the Royal Institute of Technology (KTH), Stockholm, Sweden, in 2003 and 2008, respectively.

From 2008 to 2012, he held a research position with the Automatic Control Laboratory, ETH Zurich, Zurich, Switzerland. Between 2012 and 2020, he was a Senior Scientist with the Control and Optimization Group, ABB Corporate Research, Baden-Dattwil, Switzerland. He is currently working with Totalförsvarets forskningsinstitut (FOI), Stockholm, Sweden. His research interests include switched systems, model predictive control, and control of power electronics.

Sami Pettersson (Member, IEEE) received the M.Sc. and D.Sc. degrees in electrical engineering from the Tampere University of Technology, Tampere, Finland, in 2004 and 2009, respectively.

In his dissertation, he was investigating shunt four-wire active power filter topologies and their control. Since 2008, he has been with ABB Corporate Research, Zurich, Switzerland, where he is currently working as a Principal Scientist with the Power Electronic Systems Group. Over the years, he has been part of many technology development projects as a technical specialist as well as a Project Manager in the field of power conversion technologies for various applications, such as motor drives, solar inverters, datacenters, electric vehicle charging, and active power filters. His research interests include optimized design and control of power electronic converters.

Arvid Merkert (Member, IEEE) received the Dipl.-Ing. and Dr.-Ing. (Ph.D.) degrees from Leibniz University Hannover, Hanover, Germany, in 2009 and 2017, respectively.

From 2009 to 2015, he was a Research Associate with the Institute of Drive Systems and Power Electronics, Leibniz University Hannover. Since 2016, he has been with ABB AG, Hamburg, Germany with responsibilities for the development of low voltage converter products tailored for marine applications. His research interest includes silicon carbide-based converter design.

Vivien Bergemann received the B.E. degree in electrical engineering from the Baden-Württemberg Cooperative State University, Stuttgart, Germany, in 2017 and the M.S. degree in electrical engineering from the Hamburg University of Applied Sciences, Hamburg, Germany, in 2022.

Since 2017, she has been working with ABB AG, Hamburg, Germany, with responsibilities for the embedded software development of low voltage converter products tailored for marine applications.

Lennart Harnefors (Fellow, IEEE) received the M.Sc., Licentiate, and Ph.D. degrees in electrical engineering from the Royal Institute of Technology (KTH), Stockholm, Sweden, and the Docent (D.Sc.) degree in industrial automation from Lund University, Lund, Sweden, in 1993, 1995, 1997, and 2000, respectively.

From 1994 to 2005, he was with Mälardalen University, Västerås, Sweden, and from 2001 as a Professor of Electrical Engineering. From 2001 to 2005, he was, in addition, a part-time Visiting Professor of Electrical Drives with Chalmers University of Technology, Göteborg, Sweden. In 2005, he joined ABB, HVDC Product Group, Ludvika, Sweden, where, among other duties, he led the control development of the first generation of multilevel-converter HVdc Light. In 2012, he joined ABB, Corporate Research, Västerås, Sweden, where he was appointed as a Senior Principal Scientist in 2013 and as a Corporate Research Fellow in 2021. He is, in addition, a part-time Adjunct Professor of Power Electronics with KTH. His research interests include control and dynamic analysis of power electronic systems, particularly grid-connected converters and ac drives.

Dr. Harnefors is an Editor of the *IEEE Journal of Emerging and Selected Topics in Power Electronics* and an Associate Editor of *IET Electric Power Applications*. He was the recipient of the 2020 IEEE Modeling and Control Technical Achieved Award.